JGR Solid Earth

RESEARCH ARTICLE
10.1029/2020JB019961

When There Is No Offset: A Demonstration of Seismic Diffraction Imaging and Depth-Velocity Model Building in the Southern Aegean Sea

J. Preine[1], B. Schwarz[2], A. Bauer[1], and C. Hübscher[1]

[1]Institute of Geophysics, University of Hamburg, Hamburg, Germany, [2]GFZ German Research Centre for Geosciences, Potsdam, Germany

Key Points:
- Based on waveform similarities, we surgically extract a detail-rich diffracted wavefield from zero-offset seismic data from the Aegean Sea
- Fully driven by data, we infer a laterally resolved velocity model from zero-offset information through diffraction wavefront tomography
- After interpretation-guided refinement, we derive depth-migrated reflection and diffraction images which we use for interpretation

Supporting Information:
- Supporting Information S1

Correspondence to:
J. Preine,
jonas.preine@uni-hamburg.de

Citation:
Preine, J., Schwarz, B., Bauer, A., & Hübscher, C. (2020). When there is no offset: A demonstration of seismic diffraction imaging and depth-velocity model building in the southern Aegean Sea. *Journal of Geophysical Research: Solid Earth*, *125*, e2020JB019961. https://doi.org/10.1029/2020JB019961

Received 10 APR 2020
Accepted 2 SEP 2020
Accepted article online 8 SEP 2020

Abstract A vast majority of marine geological research is based on academic seismic data collected with single-channel systems or short-offset multichannel seismic cables, which often lack reflection moveout for conventional velocity analysis. Consequently, our understanding of Earth processes often relies on seismic time sections, which hampers quantitative analysis in terms of depth, formation thicknesses, or dip angles of faults. In order to overcome these limitations, we present a robust diffraction extraction scheme that models and adaptively subtracts the reflected wavefield from the data. We use diffractions to estimate insightful wavefront attributes and perform wavefront tomography to obtain laterally resolved seismic velocity information in depth. Using diffraction focusing as a quality control tool, we perform an interpretation-driven refinement to derive a geologically plausible depth-velocity model. In a final step, we perform depth migration to arrive at a spatial reconstruction of the shallow crust. Further, we focus the diffracted wavefield to demonstrate how these diffraction images can be used as physics-guided attribute maps to support the identification of faults and unconformities. We demonstrate the potential of this processing scheme by its application to a seismic line from the Santorini Amorgos Tectonic Zone, located on the Hellenic Volcanic Arc, which is notorious for its catastrophic volcanic eruptions, earthquakes, and tsunamis. The resulting depth image allows a refined fault pattern delineation and, for the first time, a quantitative analysis of the basin stratigraphy. We conclude that diffraction-based data analysis has a high potential, especially when the acquisition geometry of seismic data does not allow conventional velocity analysis.

Plain Language Summary The active seismic method is a standard tool for studying and imaging the Earth's lithosphere. Proper imaging of complex geological targets requires seismic data of excellent quality, which are typically only acquired with expensive industrial surveys. Academic surveys, however, are often restricted to marine seismic equipment with limited illumination, which compromises imaging and interpretation. While most of the contemporary processing and interpretational routines are tailored to the reflected wavefield, recent research suggests that the often overlooked diffracted wavefield might help to overcome the gap between academic and industrial seismic imaging. Wave diffraction is the response of the seismic wavefield to small-scale subsurface structures and allows to estimate velocities even from single-channel seismic data.

In this study, we use an academic seismic profile from the southern Aegean Sea and extract a rich diffracted wavefield from the data. We utilize these diffractions to estimate a velocity model that permits a reconstruction of the subsurface in depth and specifically highlight discontinuous features related to past dynamic processes. Such depth images allow us to reliably measure thicknesses and fault angles. We conclude that diffraction-based data analysis has a high potential for academic research and strongly encourage its application in future studies.

1. Introduction

Most marine geological research during the last 50 years is based on academic seismic reflection data, collected with single-channel systems or multichannel seismic cables with an offset-depth ratio too small for velocity analysis based on common-midpoint (CMP) processing. Without doubt, the scientific outcome from those studies is impressive, yet seismic depth sections would be required in order to test them

by quantitative modeling. In recent works, it has been shown that diffractions possess unique properties which bear the potential to overcome these characteristic limitations of academic studies (e.g., Bauer et al., 2017; Fomel et al., 2007; Schwarz & Gajewski, 2017). Wave diffraction occurs at geodynamically important structures like faults, pinch-outs, erosional surfaces, or other small-scale scattering objects and encodes subwavelength information on the scattering geometry (e.g., Landa & Keydar, 1998). Diffracted waves do not obey Snell's Law and provide superior illumination compared to reflected waves. Moreover, due to their passive-source like radiation, they encode their full multichannel response in prominent data subsets like the zero-offset section (e.g., Bauer et al., 2017; Schwarz & Gajewski, 2017). Separating the diffracted wavefield has high potential: on the one hand, it principally allows to image and analyze fault systems as well as the small-scale heterogeneity with subwavelength resolution (Berkovitch et al., 2009; Decker et al., 2015; Silvestrov et al., 2015). On the other hand, diffractions illuminate the subsurface in such a way that laterally resolved velocity information can be obtained. Consequently, and without the need for expensive industry-style acquisitions, diffractions offer the possibility to measure curvatures in the zero-offset section, which allows automatic depth-velocity model building by means of wavefront tomography (Bauer et al., 2017; Duveneck, 2004). However, apart from Bauer et al. (2018) and Bauer et al. (2020), no example of data-driven depth-velocity model building based on diffraction-only data in the zero-offset domain has been published so far.

In this work, we use an academic seismic profile from the Santorini-Amorgos Tectonic Zone (SATZ), located in the South Aegean Sea, to explore the diffracted wavefield and to estimate an interval velocity model for depth conversion. The SATZ is a typical example for the aforementioned dilemma academic science is often facing. While this area is notorious for its catastrophic volcanic eruptions, earthquakes, and tsunamis, the acting tectonic forces are not completely understood to this day. One reason is that previous studies have been based on single-channel or low-fold seismic vintage data with short streamers (Hübscher et al., 2006; Nomikou et al., 2018; Perissoratis, 1995), thus handicapping the estimation of interval velocities for depth migration. Hübscher et al. (2015) and Nomikou et al. (2018) have shown that the SATZ is characterized by a high degree of local heterogeneity, e.g., in the form of abundant fault systems and volcanic intercalations, which makes this area a natural laboratory for studying diffractions.

2. Geological Setting

The SATZ represents a zone of NE-SW oriented en-echelon rifts located in the center of the Hellenic Volcanic Arc in the South Aegean Sea (Figure 1a) (Nomikou, Hübscher et al., 2019). Driven by the rollback of the Nubian slab, the southern Aegean Sea has experienced substantial extension (e.g., Bocchini et al., 2018; Cossette et al., 2016; Le Pichon & Angelier, 1979). The SATZ represents one of the most prominent morphotectonic features of the Cycladic Islands and separates the Cycladic Plateau toward the North and the minor Anafi-Astypalaea Plateau toward the south (Le Pichon & Kreemer, 2010; Nomikou, Hübscher et al., 2019). Bathymetric and available tectonic data of the SATZ most recently published by Nomikou, Hübscher et al. (2019) and Hooft et al. (2017) reveal a system of ridges and basins which has been interpreted as an extensional complex of tectonic grabens and horsts. To the southwest, the SATZ is characterized by the volcanic centers of Christiana, Santorini, and Kolumbo, which are responsible for numerous volcanic eruptions, including the well-known Minoan Eruption of Santorini approximately 3,600 years ago (Druitt & Francaviglia, 1992; Druitt et al., 1999; Hooft et al., 2019; Nomikou, Druitt et al., 2016). The remarkably linear alignment of the volcanic edifices highlights the fundamental control that crustal structure and tectonics have on the location of volcanic activity (Heath et al., 2019; Hooft et al., 2019; Nomikou, Hübscher et al., 2019; Nomikou et al., 2013).

Northeast of Santorini, three distinct basins have been identified by Nomikou et al. (2018): the Anhydros Basin, the Santorini-Anafi Basin, and the Amorgos Basin (Figure 1b). Seismic reflection data show that the opening of these basins most likely occurred in sudden tectonic pulses (Hübscher et al., 2015; Nomikou et al., 2016). The regional geological setting comprises alpine formations forming the basement rocks and overlying post-alpine sediments which are restricted to offshore areas between the islands and are thought to consist of marine sediments comprising turbidites, hemipelagic sediments, and volcaniclastics (Hübscher et al., 2015; Nomikou et al., 2016, 2018; Perissoratis, 1995). These sediments have transgressed the former Cycladic land, and volcanic intercalations have been identified close to the volcanic centers of Santorini and Kolumbo (Hübscher et al., 2015; Nomikou et al., 2016). Each basin is bounded by active marginal normal faults and characterized by extensive internal fault systems (Hübscher et al., 2015; Nomikou et al., 2018).

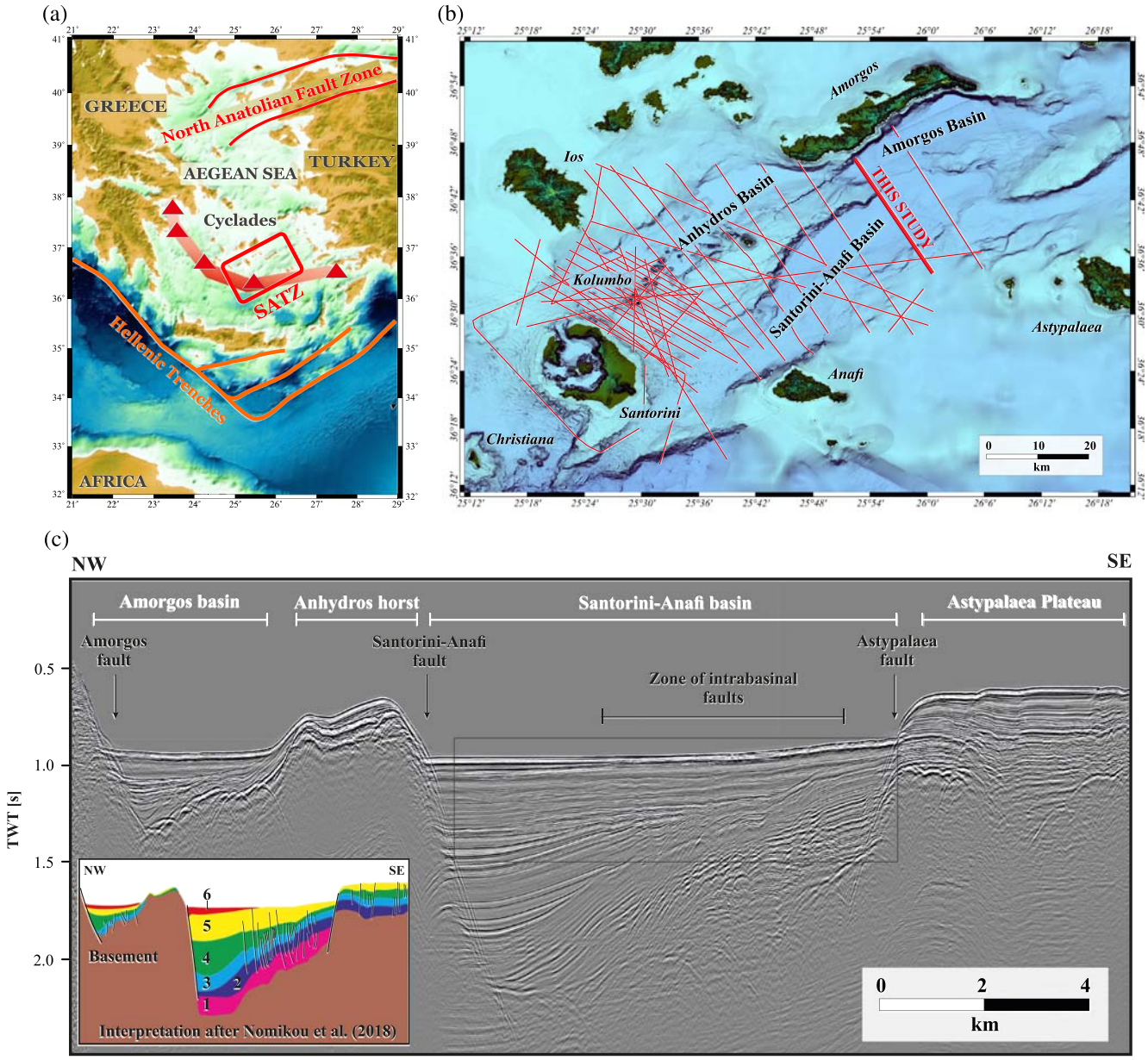

Figure 1. (a) Aegean Sea and major geological features. The semitransparent red area marks the Hellenic Volcanic Arc, and the red box indicates the working area. (b) Morphological map of the study area based on swath bathymetry. Thin red lines illustrate the location of the seismic profiles acquired during research cruise POS338 (Hübscher et al., 2006). The thick red line indicates profile 11, which is the focus of this study. (c) CMP Stack of seismic profile 11 after multiple elimination with the interpretation by Nomikou et al. (2018). The black rectangle indicates the location of the blow-up highlighted in Figure 3.

Based on a recent active seismic tomography experiment, Heath et al. (2019) and Hooft et al. (2019) obtained tomographic *P*-wave velocity models for the upper crustal structure across Santorini Volcano and the surrounding region. In agreement with the previous tectonic models, they conclude that tectono-magmatic lineaments control magma emplacement at Santorini and Kolumbo and that the initiation of basin formation predates the onset of volcanism. Heath et al. (2019) inferred that the Anhydros Basin is of maximum 1.5-km thickness and the Santorini-Anafi Basin of maximum 2-km thickness.

There is an ongoing debate about the role of strike-slip deformation in the SATZ. Based on the investigation of microseismic activity, Bohnhoff et al. (2006) concluded that the SATZ is currently influenced by a right-lateral transtensional tectonic regime. Sakellariou et al. (2010) proposed the concept that the whole

SATZ represents a shear zone characterized by dextral strike-slip to oblique faults. Direct seismic indicators like flower structures, however, have not been presented so far. Also, recent publications by Hübscher et al. (2015) and Nomikou et al. (2018) did not find direct indicators for strike-slip faulting in the presented multichannel reflection seismic data. While the possibility of strike-slip faulting was not ruled out, these authors concluded that normal faulting as a result of the regional extensional to transtensional movement represents the main tectonic mechanism.

3. Imaging Challenges

In order to further investigate the role of strike-slip tectonics and to understand the dynamics of the basin formation, seismic imaging in depth is necessary to properly estimate sedimentary thicknesses, calculate fault angles, and quantify horizontal strain. To arrive at accurate reconstructions in depth, precise velocity models, which require borehole information and lateral illumination, are in demand. Typically, this is achieved by means of of deploying long streamers as they are used, e.g., in hydrocarbon industry. Academic surveys, however, are often very limited in terms of budget, and therefore, mostly smaller streamer systems with lower channel counts are used aggravating the estimation of interval velocities.

This dilemma also applies to the SATZ. On the one hand, there are no exploitable boreholes in the area that could serve as a reliable source for velocity information. On the other hand, available academic reflection seismic data from the SATZ are generally of poor quality. Pioneering work by Perissoratis (1995) was based on analog data acquired with a single-channel streamer, and even recent studies by Sakellariou et al. (2010) and Tsampouraki-Kraounaki and Sakellariou (2018) were based on digital single-channel seismic data. In contrast, the stratigraphic studies by Hübscher et al. (2015), Nomikou et al. (2016, 2018), and Nomikou, Hübscher et al. (2019) were based on multichannel seismic data collected in 2006 during research cruise POS338 with RV Poseidon using a streamer of 600-m length (Hübscher et al., 2006). While the resulting data quality was superior compared to previous studies, the relatively large channel spacing of 25 m limited a detailed investigation of internal reflection and fault patterns, and the limited streamer length hampered the estimation of velocities from the data. Another source of uncertainty of these data regarding the estimation of interval velocities is the fact that no birds were used during the measurement to control the depth of the streamer.

Therefore, the only available velocity information from the SATZ are the tomographic *P*-wave velocity models presented by Heath et al. (2019) and Hooft et al. (2019). While these models are well suited to study the large-scale structure of the upper <3-km crust, they do not resolve the small-scale velocity distribution and do not account for the high degree of local complexity in the rift basins. Consequently, these velocity models cannot be used directly for depth migration.

Figure 1c shows a CMP stack of seismic line 11 from the POS338 data set after the application of surface-related multiple elimination (SRME) (Verschuur et al., 1992). This profile has been interpreted by Nomikou et al. (2018) and runs NW-SE crossing the Amorgos Basin, the Anhydros Horst as well as the Santorini-Anafi Basin, and the Astypalaea Plateau. The Amorgos Basin is interpreted as a semigraben produced by the activity of the Amorgos Fault, whereas the Santorini-Anafi Basin represents an asymmetric graben bounded by the important Santorini-Anafi Fault and the Astypalaea Fault (Nomikou et al., 2018). Six sedimentary units were identified within the Santorini-Anafi Basin, and major internal deformation is indicated by extended fault systems in the sedimentary strata of the Santorini-Anafi Basin within the hinge zone of the marginal Santorini-Anafi Fault and the Astypalaea Fault (see small illustration in Figure 1c). These fault systems are associated with a high number of diffractions which are overprinted by the dominant reflected wavefield. The abundance of diffractions makes this seismic profile a highly suitable example to test how the diffracted wavefield can contribute to the processing and interpretation of offset-limited academic seismic data.

4. Methods

In recent decades, detail-rich seismic wavefields have been captured on land and on the sea. Owing to its first development and extensive utilization in the prospection of oil and gas, until the early 2000s, the seismic method put most emphasis on the reflected portion of this wavefield, which resulted in many important discoveries in industry and academia. With the advent of full-waveform inversion, the desire to record low-frequency diving waves led to a spectacular yet cost-intensive shift in data acquisition (Morgan

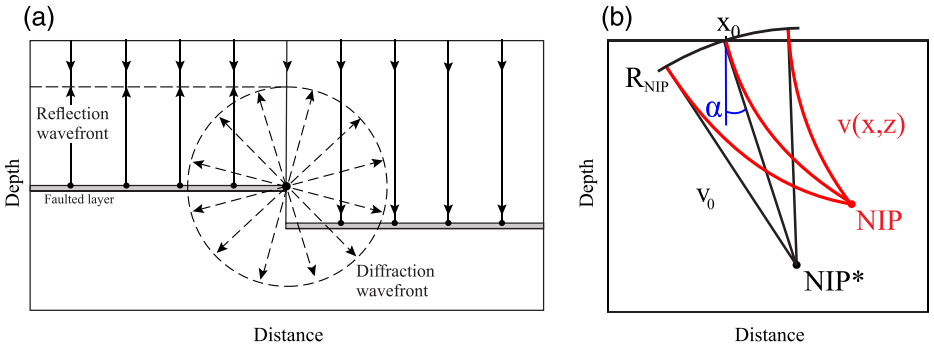

Figure 2. (a) Zero-offset rays hitting a faulted layer. While reflected wavefronts obey Snell's Law, diffracted wavefronts are scattered radially when encountering the truncated end of the faulted layer. (b) Illustration of the concept of wavefront tomography. Black lines indicate the optical image space with a medium of constant velocity v_0, in which the apparent location of the normal incident point (NIP*) is found by straight-ray projection. Determining the true velocity model $v(x, z)$ and finding the true normal incidence point (NIP) location (red) are the goals of wavefront tomography.

et al., 2013; Virieux & Operto, 2009; Warner et al., 2013). As a result, the promised resolution of such reconstructions remains largely intractable in expeditions where academic objectives are concerned. To arrive at maximally resolved seismic subsurface reconstructions when academic low-fold and short-offset acquisitions were recorded, we make use of the still largely unexplored diffracted component of the wavefield (e.g., Schwarz, 2019b). As illustrated in Figure 2a, diffractions are unique in that they exclusively occur when subsurface properties change abruptly. More precisely, in contrast to reflections and diving waves, these signatures are only caused, when the local curvature of a material contrast is comparable to or even smaller than the prevailing seismic wavelength.

4.1. Diffraction Separation and Focusing

Owing to the effect of geometrical spreading, diffractions are generally characterized by very low amplitudes and often remain masked by more prominent higher amplitude reflections (Figure 2a). For that reason, accessing the diffracted wavefield has been and still remains a major challenge to confront. In recent years, a range of methods has been introduced to arrive at approximate diffraction-only images based, e.g., on modified versions of Kirchhoff's diffraction integral (e.g., Dafni & Symes, 2017; Moser & Howard, 2008; Yin & Nakata, 2017), specific versions of the Radon transformation and plane-wave destruction filters (e.g., Fomel, 2002; Karimpouli et al., 2015), or multidimensional stacking (Bakhtiari Rad et al., 2018; Bauer et al., 2016; Dell & Gajewski, 2011). While the latter has the advantage of being directly applicable in the time domain without the need for specific data transformations and not requiring a detailed velocity model, the quality of the separation depends on the quality of the performed coherence measurements and the prestack data.

A different approach to the problem was introduced by Schwarz and Gajewski (2017) and extended by Schwarz (2019a). In contrast to previous attempts, these works specifically target the reflected rather than the diffracted wavefield, with the potential benefit of leaving weak diffracted signatures largely unharmed in the separated result. Likewise, in contrast to workflows directly incorporating Kirchhoff migration, the separation is performed directly in the unmigrated (data) domain, leading to the applicability of a multitude of conventional imaging and inversion algorithms. The first step of this noninvasive strategy, very much like in surface-related multiple suppression (Verschuur et al., 1992), constitutes in a targeted *modeling* of the interfering noise—in our case, the reflected contributions. This is achieved by means of coherence analysis, in which the local fit of a curved traveltime operator,

$$\Delta t(x_0, t_0) = \sqrt{\left(t_0 + 2\frac{\sin\alpha}{v_0}\Delta x\right)^2 + \frac{2t_0\cos^2\alpha}{v_0}\left(\frac{\Delta x^2}{R_N} + \frac{h^2}{R_{NIP}}\right)} - t_0, \quad (1)$$

is optimized for neighboring traces (with midpoints laterally separated by Δx and half the source-receiver distance h), by repeatedly evaluating the semblance norm (Neidell & Taner, 1971). Written as above, the estimated propagation time $t_0/2$, the emergence angle α, and the curvature radius R_{NIP} represent one-way properties of a wavefront emitted by a fictitious source placed either at the normal-incidence point (NIP)

or the diffractor location (compare Figure 2). While for reflections, this wavefront is fully conceptual and expresses a symmetry in the CMP gather ($h \neq 0$), for diffractions and passive events ($R_N = R_{NIP}$), it describes the shape of the actual physical wavefield stemming from the localized scatterer or the passive source (Bauer et al., 2017; Diekmann et al., 2019). As a result, for reflections, sufficient offset (h) information is needed, whereas, for diffractions, wavefront curvatures can be fully determined in the zero-offset ($h = 0$) section. Forming a by-product of coherence analysis, these wavefront attributes, in addition to velocity inversion, permit the formulation of supportive diffraction filters that can additionally constrain the separation (Schwarz, 2019a; Schwarz & Gajewski, 2017).

Following this procedure of constructing a reflection model by means of local coherent data summations, a successful separation requires an adaptation step, which like the summation itself should be performed within an aperture to preserve weak interfering energy. Such an adaptation of the reflection stack is achieved by introducing local scaling coefficients γ_0 and time shifts τ_0. Following the superposition principle, the interference of reflections and diffractions can in good approximation be *reversed*, if the estimated coherent reflection model is reasonably accurate. Expressing the coherent reflection stack as C_{ref} and the raw input data as D, the adaptive separation procedure can thus be expressed as

$$C_{diff} \approx D(x_0, t_0) - \gamma_0 C_{ref}(x_0, t_0 + \tau_0), \tag{2}$$

where $(\mathbf{x}_0, t_0)$ is the central data point under consideration and C_{diff} denotes the diffracted wavefield. For more details on the estimation of the necessary amplitude weights and time shifts and applications in seismic and ground-penetrating radar data, we refer to Schwarz (2019a).

After their successful extraction, uncorrelated noise that was suppressed in the reflection model will likewise remain in the data, thereby setting natural limits on the detectability of diffracted signatures. However, as diffractions, despite their weakness, possess the property of coherence, the aforementioned coherence analysis can be carried out for the separated data set.

4.2. Wavefront Tomography

Based on the concept of wavefront attributes, Duveneck (2004) introduced wavefront tomography, an efficient and robust scheme for the estimation of smooth depth-velocity models, which has been applied successfully to industrial multichannel data (Bauer et al., 2017) as well as diffraction-only data (Bauer et al., 2017, 2018) and passive-seismic measurements (Diekmann et al., 2019; Schwarz et al., 2016). In this study, due to limited offsets in the academic seismic data, the reflected measurements are hardly usable for velocity inversion. Accordingly, wavefront attributes have to be extracted from the diffraction-only data C_{diff} obtained during the previous step. This is done by means of coherence analysis, during which the hyperbolic traveltime moveout approximation (1) is locally fitted to the data (e.g., Jäger et al., 2001). The input for wavefront tomography consists of numerous sets of wavefront attributes that can be picked in an automatic fashion in the resulting zero-offset sections based on their coherence

$$\mathbf{d}_i = (\xi, T, \alpha, R_{NIP})_i, \qquad \text{with } i = 1, \ldots, n_{picks}, \tag{3}$$

where n_{picks} denotes the total number of picked data points, $T = t_0/2$ the one-way zero-offset traveltime, and ξ the position on the recording surface. The model parameters $\mathbf{m}$ are the B-spline velocity coefficients $v(x, z)$ on a predefined grid of $n_x \times n_z$ knots and localizations $(x, z)_i$ and ray-takeoff angles θ_i associated with each data point. The initial localizations and ray-takeoff angles are obtained by downward kinematic ray tracing into the initial model (which in our applications merely consists of the constant near-surface velocity v_0, compare Figure 2b) starting from ξ_i under the angles α_i until the remaining traveltime vanishes. Subsequently, upwards dynamic ray tracing from $(x, z, \theta)_i$ yields the modeled data points $\tilde{\mathbf{d}}$. The misfit between the measured and modeled data points $\Delta\mathbf{d} = \mathbf{d} - \tilde{\mathbf{d}}$ defines the cost function,

$$\Psi(\mathbf{m}) = \frac{1}{2}\|\mathbf{d} - \tilde{\mathbf{d}}\|_2^2 + \Lambda\left(\partial_{xx} v(x, z)), \partial_{zz} v(x, z)\right), \tag{4}$$

where Λ constitutes a regularization term that ensures a smooth velocity model. During the inversion, the cost function is minimized iteratively in a damped-weighted least-squares sense until a velocity model and localizations $(x, z)_i$ are found that are most consistent with the measured wavefront attributes (compare Figure 2b). For stability, we apply the inversion algorithm in a cascaded fashion, starting from a coarse grid and then successively increasing the number of B-spline knots.

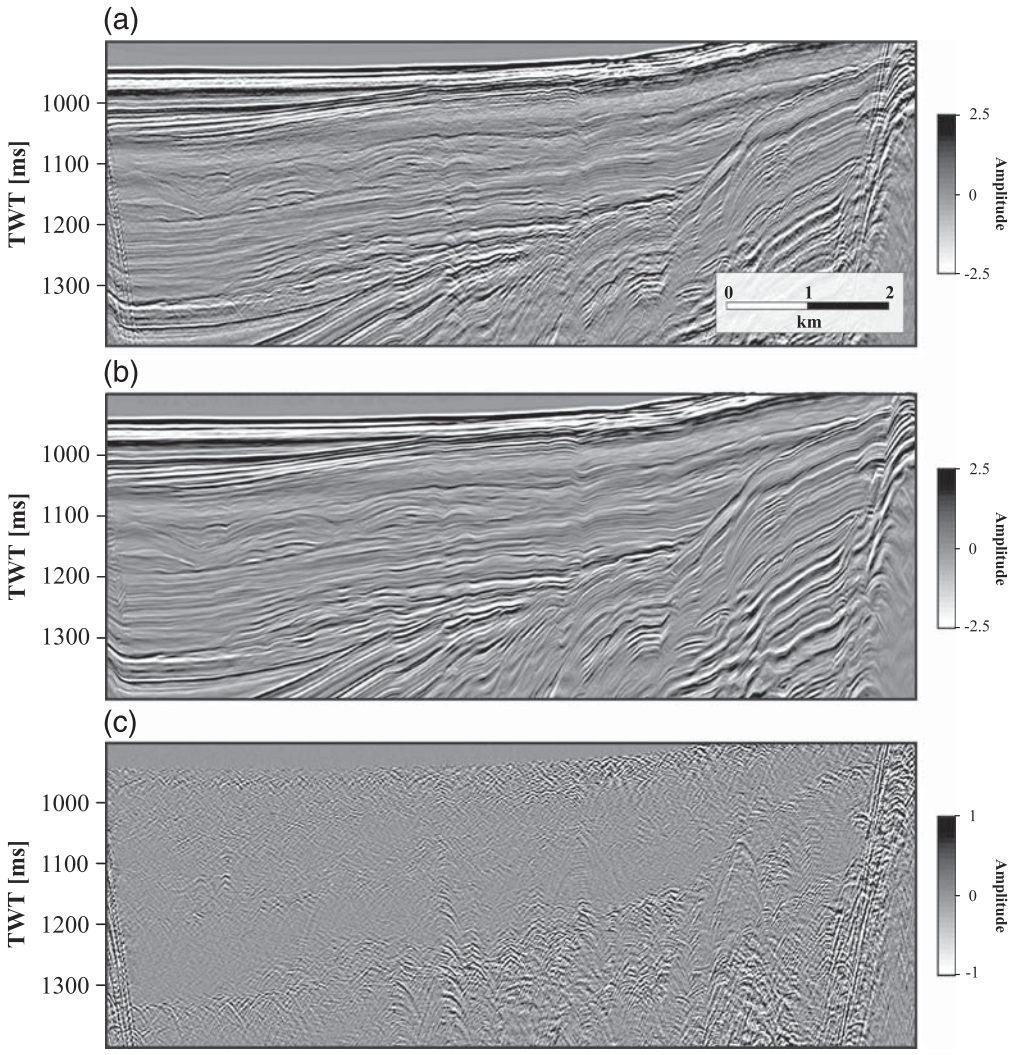

Figure 3. Results of the coherent stacking and subtraction scheme for diffraction separation illustrated on a zoomed section from seismic line 11: (a) the input CMP Stack, (b) the reflection-only data, and (c) the diffraction-only data.

5. Data-Driven Results

5.1. Diffraction Separation

In order to reveal the faint diffracted wavefield, we perform diffraction separation based on the approach by Schwarz (2019a). As input, we use the CMP stack of seismic line 11 with a CMP spacing of 12.5 m from the POS338 data set (Figures 1 and 3a). With the purpose of recovering as much of the diffracted wavefield as possible, preprocessing for the separation was kept to a minimum comprising only simple bandpass filtering for the removal of low-frequent swell noise, SRME for multiple elimination in addition to the application of a top mute and trace mute. The processing flow is illustrated in Figure S1.

In the first step, we carry out coherent wavefield summation using planar beamforming in order to estimate the reflection-only data. With a lateral aperture of 100 m and a coherence time window of 20 ms, supported by a wavefront filter with a maximum angle of 10° to search for, we obtain the reflection-only section illustrated in Figure 3b. As demonstrated by Schwarz (2019a), the lateral aperture plays an important role in the success of the modeling of the reflected wavefield as it controls the number of traces used for the coherent stacking and, consequently, how discriminative the separation is. The more traces are considered, the more of the crossing diffraction energy is neglected in the reflection-only data, and the better the diffraction-subtraction works later on. However, as too large apertures tend to smear the reflections, the proper aperture choice can bee seen as a trade-off and, consequently, requires parameter testing

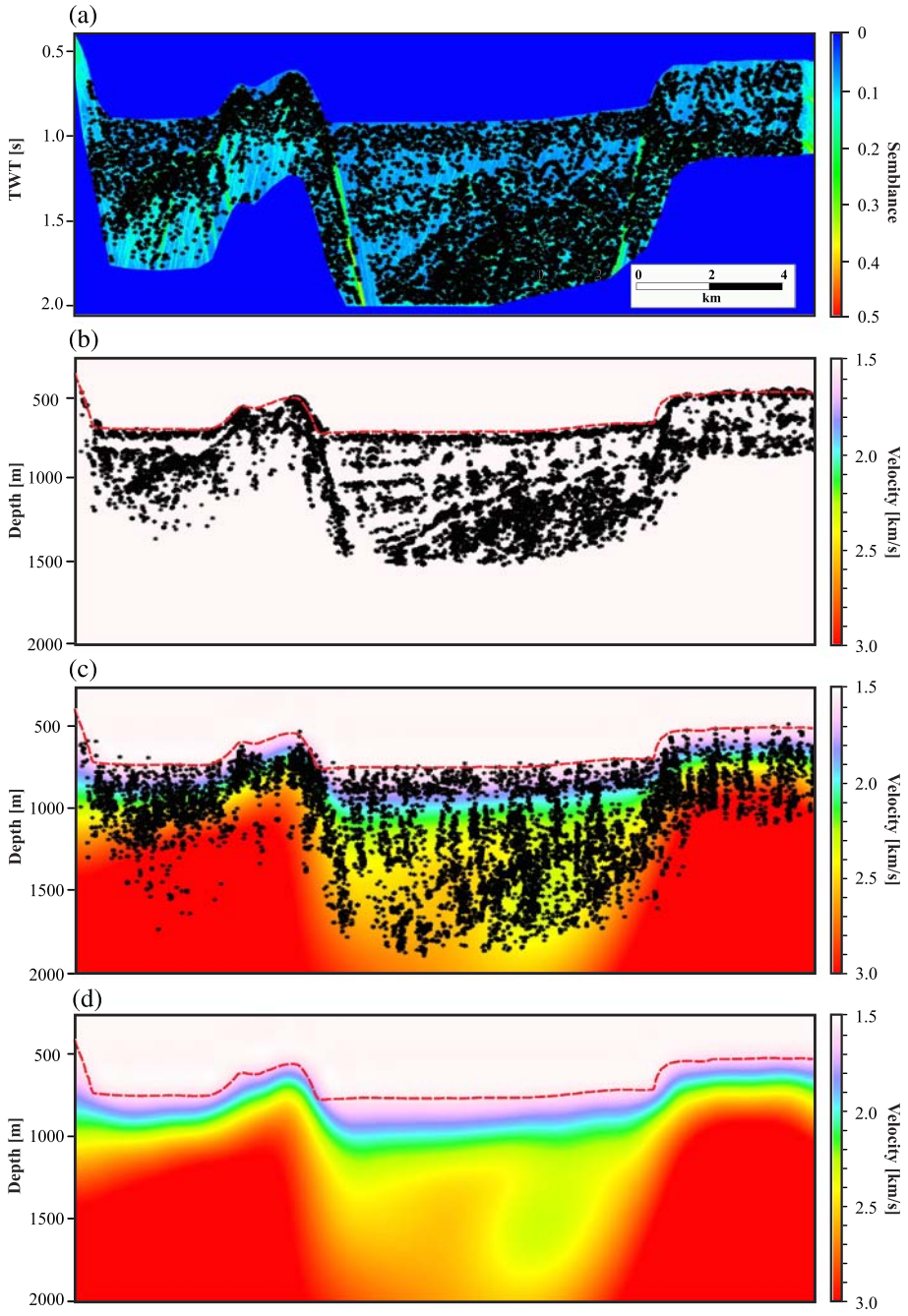

Figure 4. Results of diffraction-based wavefront tomography. (a) All 11,866 automatically picked data points plotted into the semblance section. (b) The constant initial model for the inversion overlain by the initial scatterer localizations. (c) Final velocity model overlain with final scatterer localizations. (d) Final velocity model. The dashed red line indicates the location of the seafloor horizon.

(Schwarz, 2019a). As Figure 3b demonstrates, the reflection-only section has a higher lateral continuity compared to the input CMP stack (Figure 3a) and, more importantly, is free of diffractions.

In the next step, the diffraction-only data are generated by performing coherent beam subtraction. Also here, the lateral aperture is an important parameter and several tests showed that using 400 m is the best trade-off value. An example of the effect of different apertures used for the separation is provided in the supplementary information (Figure S2). The resulting diffraction-only section is illustrated in Figure 3c. This section is generally free of reflections, and a rich, complex diffracted wavefield is revealed. Diffractions

can be identified throughout the section but seem to cluster around distinctive structures. Not only vertical structures that seem to represent faults but also horizontal structures that seem to represent unconformities are highly *diffractive*. Note, e.g., the high number of diffractions along the faults in the center of the basin and toward the marginal Astypalaea Fault. This illustration highlights that most of the diffractions at faults are created at the tips of the faulted horizons. Consequently, faults seem only diffractive when reflection horizons are present.

The numerical cost of the whole diffraction separation routine can be considered as fairly reasonable. The seismic line under consideration comprises 2,022 CMPs and was acquired with a sampling rate of 1 ms and a recording length of 3 s. On a conventional computer with a quad-core processor, the coherence analysis for deriving the reflection-only data took approximately 10 min and the adaptive subtraction for generating the diffraction-only data approximately 1 hr.

5.2. Wavefront Tomography

In order to derive a depth-velocity model, we apply the previously introduced wavefront-tomographic scheme based on the separated zero-offset diffraction response. In the first step, we estimate the wavefront attributes and the diffraction coherence using the semblance norm. Figure 4a illustrates the resulting semblance section overlain by 11,866 automatically picked data points, which consist of sets of wavefront attributes that form the input of the inversion algorithm. These data points are scattered over the whole section ensuring the needed illumination for velocity inversion. In order to avoid contributions from the faint multiple remnants, we mute the diffraction coherence below the arrival time of the seafloor multiple before the automatic picking. In the next step, we calculate the initial model without assuming any a priori information other than the near-surface velocity $v_0 = 1.52$ km/s which corresponds to the regional water velocity. The resulting initial model is displayed in Figure 4b together with the initial ray starting locations associated with each data point, which are obtained by downward kinematic ray tracing into the constant initial model. During the inversion, we applied two grid refinements, the first nine iterations with 11×5 B-spline knots and a spacing of 2,500 m in x-direction and 625 m in z-direction, followed by eight iterations with 21×9 B-spline knots (1,250 m in x-direction and 312.5 m in z-direction) and seven iterations with 41×17 B-spline knots (625 m in x-direction and 156.25 m in z-direction). The resulting velocity model overlain with the final scatterer locations after a total of 24 iterations is illustrated in Figure 4c. While the scatterer locations were distributed quite broadly in the semblance section, the final scatterer locations seem to be more focussed after the inversion. We identify several areas where the final scatterer locations organize in vertical structures following the outline of faults.

Figure 4d shows the velocity distribution inferred from the diffracted wavefield. The inverted velocities range from 1.5 to 3.0 km/s. The basement is estimated at approximately 3.0 km/s, while for the sedimentary strata, a rather smooth velocity increase from 1.5 to approximately 2.5 km/s has been inverted. In general, the velocity model acknowledges the expected velocity contrast from the sedimentary strata to the basement very well. Especially the elevated basement of the Anhydros Horst is distinctly expressed in the velocity model. The velocity distribution in the Santorini-Anafi Basin is characterized by a lateral velocity increase between the left and the right part of the basin. While the inverted velocities in the right part do not exceed 2.5 km/s, high velocities of over 2.9 km/s can be found within the sedimentary strata of the left part of the basin. In contrast to that, the velocity distribution for the Astypalaea Plateau and the Amorgos Basin shows no comparable lateral velocity variations.

5.3. Depth Imaging

In the next step, we use the data-derived velocity model for finite-difference (FD) depth migration. As input for the migration, we use the zero-offset section after multiple elimination which has also been used as input for diffraction separation (see Figure S1). The result is displayed in Figure 5a and a comparison of the migration result with the depth-stretched CMP stack is provided in Figure S3. In general, the quality of the depth image seems good as most faults are sharply focussed and there are no obvious artifacts. Also, the rugged basement reflection is well imaged and all of its many edges are sharply focused. While the margins of the Santorini-Anafi Basin are reconstructed reasonably well, we observe a slight down-bending of the seafloor reflections toward the Anhydros Horst and the Astypalaea Plateau which could be explained as a consequence of the smoothness of the velocity model.

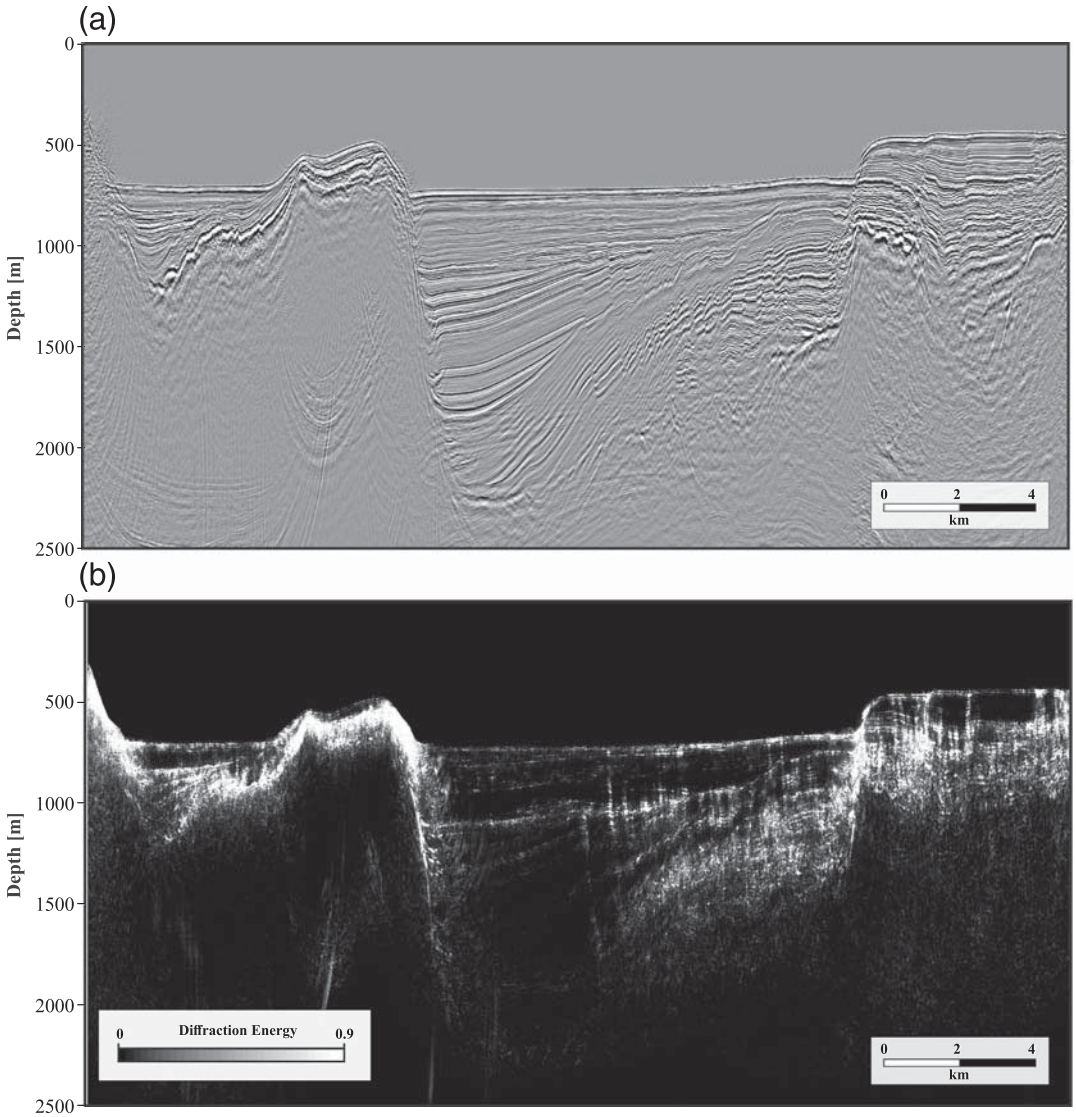

Figure 5. (a) Finite-difference depth migration of the full wavefield using the velocity model illustrated in Figure 4d. (b) Diffraction energy calculated from the finite-difference depth-migrated diffraction-only data using the inverted velocity model illustrated in Figure 4d.

In addition, we present a diffraction depth image of the profile obtained by means of FD depth migration of the diffraction-only data using the inverted velocity model. By calculating the squared envelope of the migrated diffractions, we arrive at an image that illustrates the *diffraction energy* (Figure 5b). Such a diffraction depth image provides highly resolved structural detail. In particular, it highlights the complex system of internal faults in the center of the Santorini-Anafi Basin and on the Astypalaea Plateau. These faults are expressed as linear, slightly curved features, and can be traced nicely through the seismic section and seem to penetrate the seafloor on the Astypalaea Plateau. Furthermore, we observe that the Anhydros Horst is associated with a high degree of diffractivity, possibly as a consequence of tectonic exposure or erosion. Interestingly, some unconformities can be clearly delineated in the diffraction image, while others are expressed as faint or even transparent events which suggests a different roughness associated with these horizons.

6. Interpretation-Driven Refinement

6.1. Quality Control

As mentioned in the previous section, the data-derived velocity model presented in Figure 4d depicts the expected velocity distribution of the profile quite well. The sedimentary strata are generally associated with

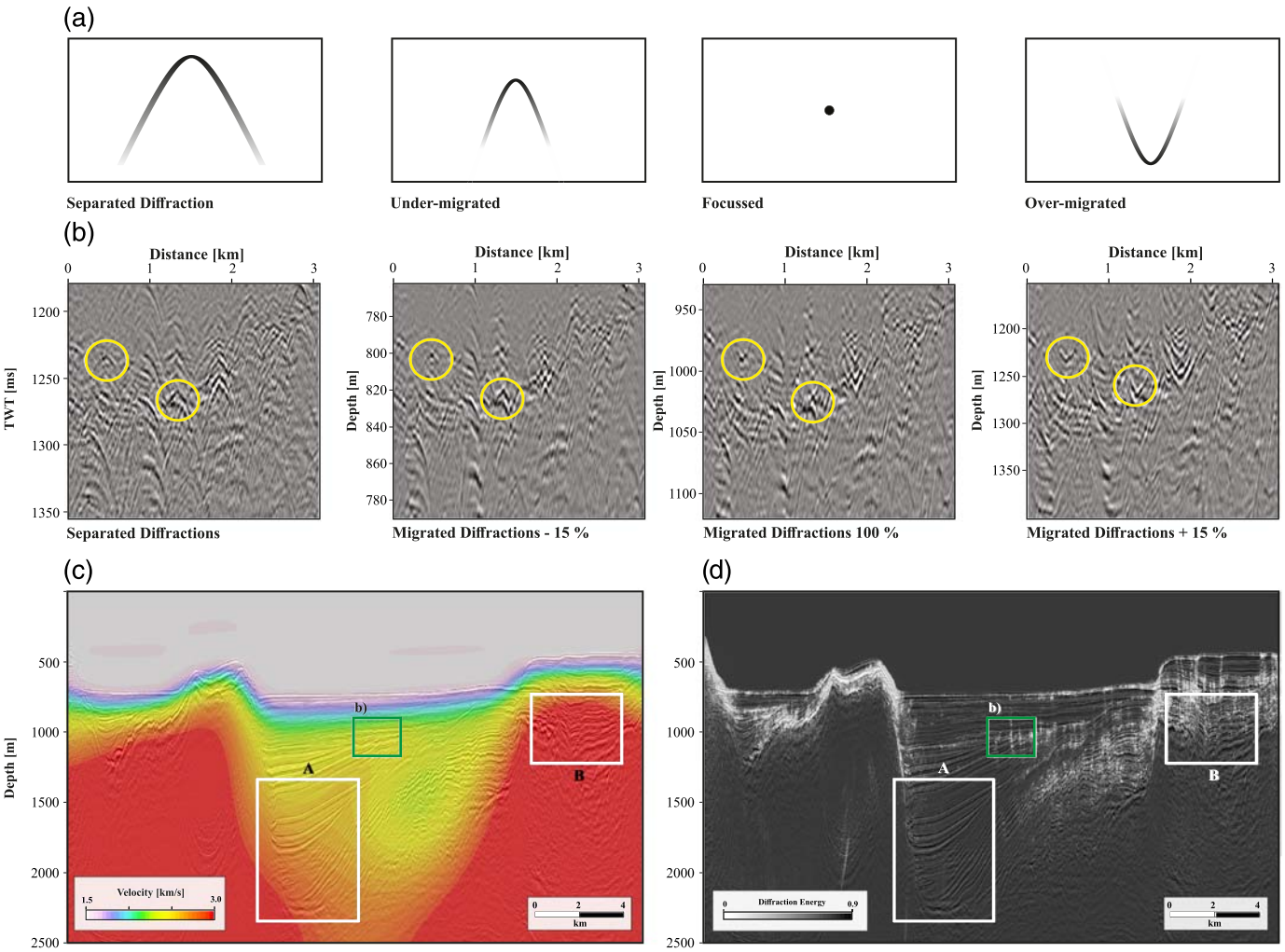

Figure 6. (a) Schematic illustration of how migration with different velocities affects the shape of diffractions. (b) A small excerpt of the seismic section after diffraction separation. Migration with different velocities results in undermigration (−15%), focusing (100%), or overmigration (+15%). Two prominent instances are highlighted by the yellow circles. (c) FD migrated seismic section overlain with the inverted velocity model and (d) the diffraction depth image. White rectangles indicate areas of unexpected high velocities within the sedimentary strata. The green rectangle indicates the location of the small excerpt shown in (b).

a rather gentle velocity increase from approximately 1.5 to 2.5 km/s, while the basement is associated with higher velocities in the order of 3.0 km/s. These values are mostly in agreement with the regional tomographic model presented by Heath et al. (2019), who attribute metamorphic basement and sedimentary strata with to velocities higher or lower than 3.0 km/s, respectively (compare their Figure 5). However, a more detailed comparison of their results is not feasible as the presented velocity models are too coarsely resolved considering the high complexity of the data under consideration.

In order to further assess the quality of our velocity model, we (i) analyze the focusing of diffractions after migration and (ii) evaluate the geological plausibility of the inverted velocities. In a similar way to the velocity analysis of conventional long-offset data, where the flatness of common-image-gathers (CIGs) is used for quality control, we visually assess the focusing behavior of diffractions to evaluate the quality of the velocity model. Figure 6a shows a schematic illustration of how diffractions appear after the migration with different velocities. If too low velocities are used, the diffractions will be undermigrated and have downward bent tails. If the velocity used for the migration is correct, the diffractions will be focussed. Using too high velocities results in overmigration and upward bent diffraction tails.

Following this strategy, we evaluated the behavior of the separated diffractions after migration with the inverted velocity model and with velocity models perturbed by ±15%, respectively. An excerpt from the

result containing numerous diffractions is illustrated in Figure 6b (see Figure 6c for the location within the profile). Two prominent instances are emphasized by the yellow circles. Migrating the separated diffractions with a velocity model of −15% of the inverted velocity model leads to a narrowing of the diffraction tails, but they remain visible in the section. In contrast to that, the migration of the diffractions with the inverted velocity model leads to an overall focusing, and the section appears generally free of diffraction tails. The migration with +15% leads to an overmigration of the diffractions, and we can identify numerous upward bent diffraction tails within the seismic section. These observations show that the inverted velocity model fits the data quite well and can be validated at least with an approximate confidence interval of ±15%.

By applying this quality control procedure throughout the seismic section, we were able to validate the inverted velocities for most of those areas, in which distinct diffractions are present, e.g., along faults. In areas where the diffracted wavefield is more complex, however, focussing is more complicated to assess quantitatively. Especially in the vicinity of the alpine basement, we cannot be certain that we take only point diffractions into account as we might encounter lenticular objects (Malehmir et al., 2009). In addition, the focusing of diffractions is only an appropriate quality control tool if scattering occurs in or close to the acquisition plane. However, in case of out-of-plane scattering, diffraction focusing is not an appropriate measure for quality control. As such diffractions appear with distorted curvatures, they will also affect the quality of the velocity inversion. As shown by Malehmir et al. (2009), such out-of-plane diffractions can contribute from considerable distances from the acquisition plane. The identification of out-of-plane contributions still constitutes a challenge, and we have to assume that our estimates are affected by them. We argue, however, that the inverted velocities from the diffracted wavefield can be expected to be reliable when a high density of diffractions, e.g., from elongated faults is encountered. It is reasonable to assume that such structures are most likely to be located in the acquisition plane and, consequently, diffraction focusing can be used for quality control in these areas. In contrast, inverted velocities in areas that are constrained by few events should be assessed with caution.

Therefore, we use a second criterion for evaluating the quality of the inverted velocity model: the geological plausibility. Figure 6c illustrates the depth-migrated section overlain with the inverted velocity model and Figure 6d shows the depth-migrated section overlain with the diffraction depth image. We observe considerable lateral velocity variation within the Santorini-Anafi Basin. In the right part of the basin, the velocities of the sedimentary strata are generally lower than 2.5 km/s, while in the left part of the basin, we observe a zone with high velocities exceeding 2.9 km/s as highlighted by Rectangle A. Those velocities can be considered geologically implausible for the expected marine sediments (Nomikou et al., 2018). As can be seen in Figure 6d, this area is mostly free of diffraction events. This lack of illumination might explain why implausibly high velocities have been inverted here. If an area is not properly constrained by diffractions, the inverted velocity model is more likely to suffer from interpolation artifacts or wrongly fitted events. However, the right part of the basin is characterized by a high degree of diffractivity, which makes the respective velocity better supported by data.

Furthermore, Rectangle B highlights an area with high velocities in the center of the Astypalaea Plateau. Here, the contact of the basement and the sediments is not properly acknowledged by the inverted velocity model and the lower sedimentary strata are associated with velocities of approximately 3.0 km/s, which, again, seems not plausible here. The margins of the plateau, however, are associated with lower velocities and honor the contact of the basement and the sediments more accurately. In contrast to the region denoted by Rectangle A, Figure 6d indicates that the area within Rectangle B is actually constrained by numerous diffractions. However, we know from Nomikou et al. (2018) that the Astypalaea Plateau is a complex region with a highly varying sedimentary thickness and a very rugged basement. Therefore, the probability of out-of-plane contributions is high in this area, which could explain why unrealistically high velocities have been inferred.

These observations highlight the two main limitations of the proposed velocity inversion workflow for 2D seismic acquisitions: the lack of diffractions in some regions and out-of-plane contribution. However, if 3D data are considered, the problem of out-of-plane can be addressed (e.g., Bauer et al., 2020). Other limitations of the data-driven velocity estimation are the fact that it does not account for anisotropy and that smoothing does not account for the strong velocity contrasts, e.g., at the contact of the basement and the sedimentary strata. This would explain, e.g., the previously mentioned down-bending of the seafloor reflection close to the Anhydros Horst in the migrated section (Figure 5a).

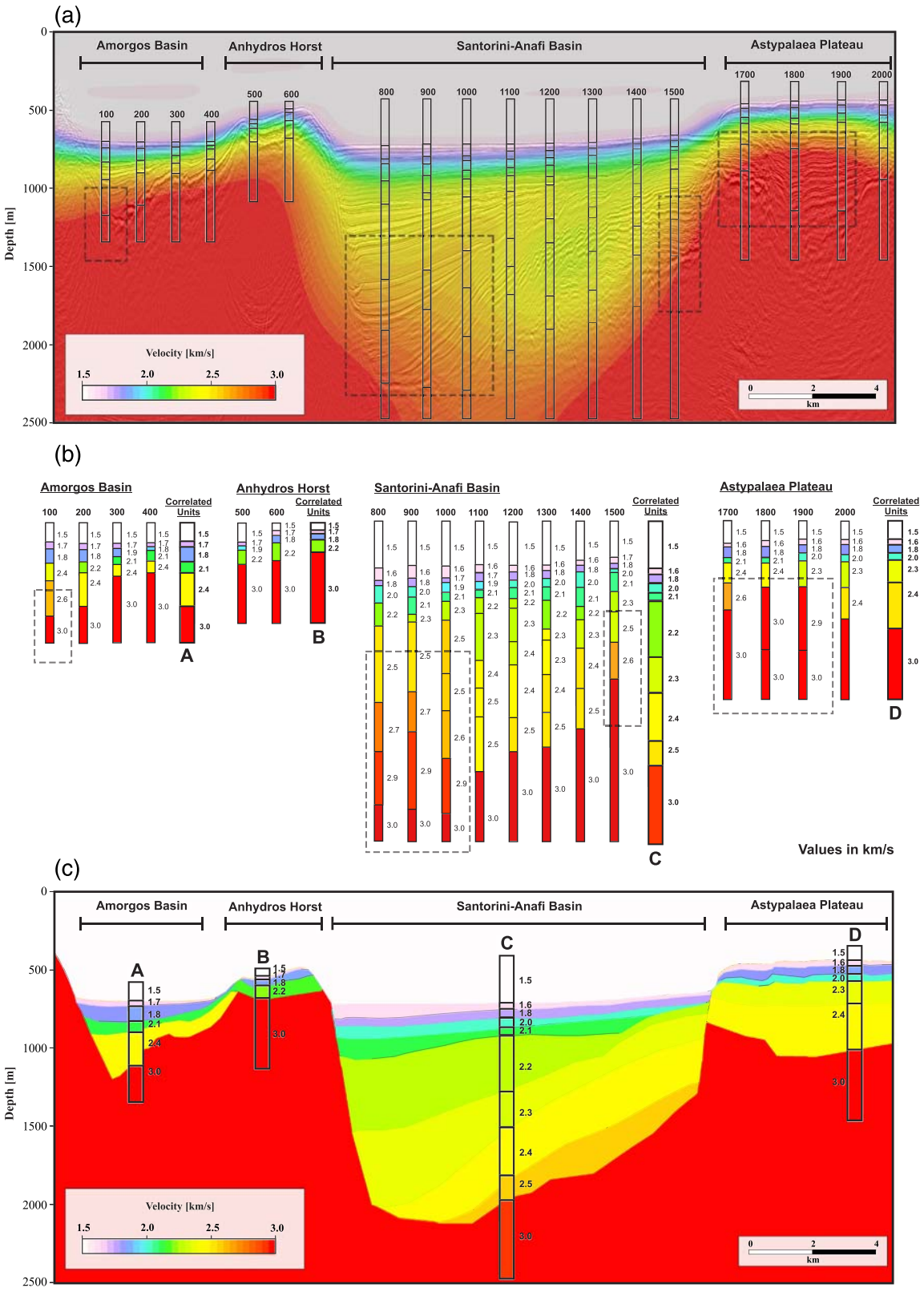

Figure 7. Illustration of the interpretation-driven velocity refinement. (a) FD-migrated seismic section overlain with the inverted velocity model and our sampling points. (b) Extracted velocity values for each stratigraphic layer and the correlated units. The dashed rectangles highlight those areas where our quality control indicated implausible velocities. (c) Refined velocity model.

6.2. Velocity Model Refinement

Although our quality control showed that the data-derived velocity model is reliable in extended regions, in certain areas, the velocities are implausible for the previously explained reasons. In order to derive a velocity model that is geologically consistent throughout, we suggest an interpretation-driven refinement that utilizes the strengths of the data-driven velocity inversion to compensate for its weaknesses.

Therefore, our strategy is to extract 1D velocity profiles for every 100th CMP from the inverted velocity model and to assign the extracted velocities to stratigraphic units. This procedure is illustrated in Figures 7a and 7b. The dashed rectangles highlight those areas, where our quality control indicated zones of implausible velocities. For each layer, we estimate the average value of the extracted velocity and round this estimate to the second decimal place. Afterward, we correlate the units within each compartment of the seismic profile and determine a mean value for the respective stratigraphic layer, while excluding all values within the predefined zones of uncertainty. The resulting correlated units for each compartment are illustrated in Figure 7b.

In the next step, we assemble a velocity model for the whole seismic section based on the correlated units. The resulting model is depicted in Figure 7c. Apart from the zones of high uncertainty, the resulting velocity model is comparable to the original data-driven inversion. For each compartment, the refined velocity model fits the stratigraphic interpretation by Nomikou et al. (2018) reasonably well. In general, the velocity model consists of an upper layer with rather low-velocities of approximately 1.6–1.7 km/s underlain by a layer with an interval velocity of approximately 1.8 km/s. Below these upper units, we identify several intermediate units with velocities in the order of 2.0–2.2 km/s which are comparably thin for most parts of the profile but have a large thickness in the Santorini-Anafi Basin. The lowermost units comprise velocities of approximately 2.4 km/s. Although a comparison is only partially feasible, this refined velocity model is in general agreement with the regional tomographic model presented by Heath et al. (2019) while remaining geologically plausible. However, just like any other means of interpretation, the whole refinement process is subject to a certain degree of subjectivity and does not account for lateral velocity variations within the compartments of the seismic section, e.g., as a result of compaction. It might be stressed at this point that the proposed interpretational guide is informed by the lateral continuity of the reflected wavefield, which emphasizes the distinct yet complementary nature and synergetic potential of reflections and diffractions for imaging.

6.3. Geological Implications

Figure 8a shows the FD depth-migrated seismic section overlain with the refined velocity model. This illustration highlights the geological plausibility of the velocity model. Since the refined velocity model takes into account the high velocity contrast between the metamorphic basement and the sedimentary strata, the depth-migrated image is now free of artifacts such as the warping of the seafloor reflection, which had been observed after the migration with the data-driven velocity model (Figure 5a). A comparison of the FD depth-migrated image using the refined velocity model and the velocity model derived from wavefront tomography can be found in Figures S4 and S5. The overlay of the velocity model and the seismic section further suggests a stratigraphic relationship of the lowermost units of the Amorgos Basin, the Santorini-Anafi Basin, and the Astypalaea Plateau.

Figure 8b illustrates the refined FD depth-migrated image as well as the dipping angles and throws of the most significant faults. Based on this depth image, we infer the total thickness of the sedimentary strata to be approximately 1.4 km, which is remarkable considering that the marine sediments of the SATZ are considered to be of Plio-Quaternary age (Perissoratis, 1995). In order to understand the acting forces responsible for the formation and the evolutionary history of this rift zone, it would be very helpful to estimate the amount of extension. Having derived a depth-converted seismic section, we encourage the application of structural restoration (Nunns, 1991) in future studies in order to reconstruct and measure the extension in the Santorini-Anafi Basin.

Using the interpretation-software KINGDOM, we measure the angles and throws of the most significant faults as illustrated in Figure 8b. Compared to the estimates by Nomikou et al. (2018), our study indicates smaller angles for the marginal Amorgos Fault (30° compared to 38°) and the listric Santorini-Anafi Fault (40–58° compared to 68°) and a larger angle for the Astypalaea Fault (64° compared to 45°) but still indicates normal faulting to be the main tectonic mechanism responsible for basin formation. While the throw of the

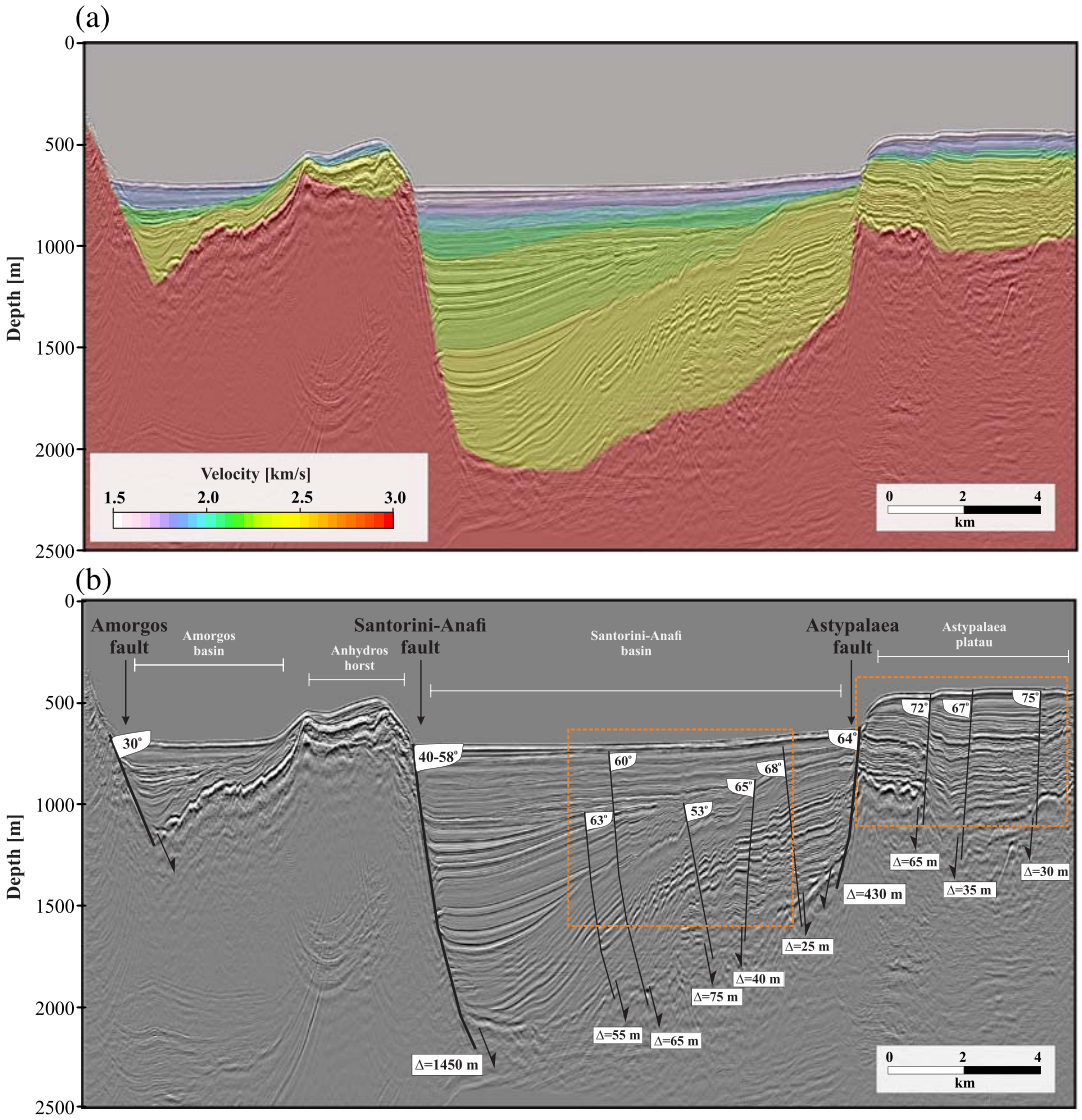

Figure 8. (a) Full-wavefield depth image superimposed by refined velocity model used for migration. (b) Depth image as in (a) but shown with dipping angles and throws estimated for the most prominent faults. Orange rectangles announce two sections that are highlighted in Figure 9.

marginal faults is very significant (approximately 1,450 m for the Santorini-Anafi Fault and approximately 430 m for the Astypalaea Fault), the throw of the most important internal faults ranges from 25 to 75 m. Their fault angles lie between 53° and 75°. As indicated in Figure 8b, the sense of displacement of the internal faults within the center of the Santorini-Anafi Basin changes from NW to the SE forming narrow subsided zones in the center. In order to further analyze the internal fault systems, we utilize the diffraction depth image derived with the refined velocity model. As shown in Figure 5b, such diffraction images highlight small-scale heterogeneity and seem to be good indicators for faulting, tectonic overprint, or erosion.

As already mentioned by Schwarz (2019a), diffraction images are highly suitable to be used as an alternative to conventional attributes for fault interpretation as, e.g., image coherence or image curvature (Bahorich & Farmer, 1995; Chopra & Marfurt, 2007; Marfurt et al., 1998). Following this notion, we combine the diffraction depth images and the refined depth images to arrive at physically informed laterally resolved discontinuity maps. Two examples of these maps are illustrated in Figure 9 for the Astypalaea Plateau (a–c) and the intrabasinal fault system of the Santorini-Anafi Basin (d–f). By blending the diffraction image with the depth-migrated images, we are able to combine the strengths of both the reflected and the diffracted wavefield to facilitate the identification of faults. Especially when considering highly complex fault systems

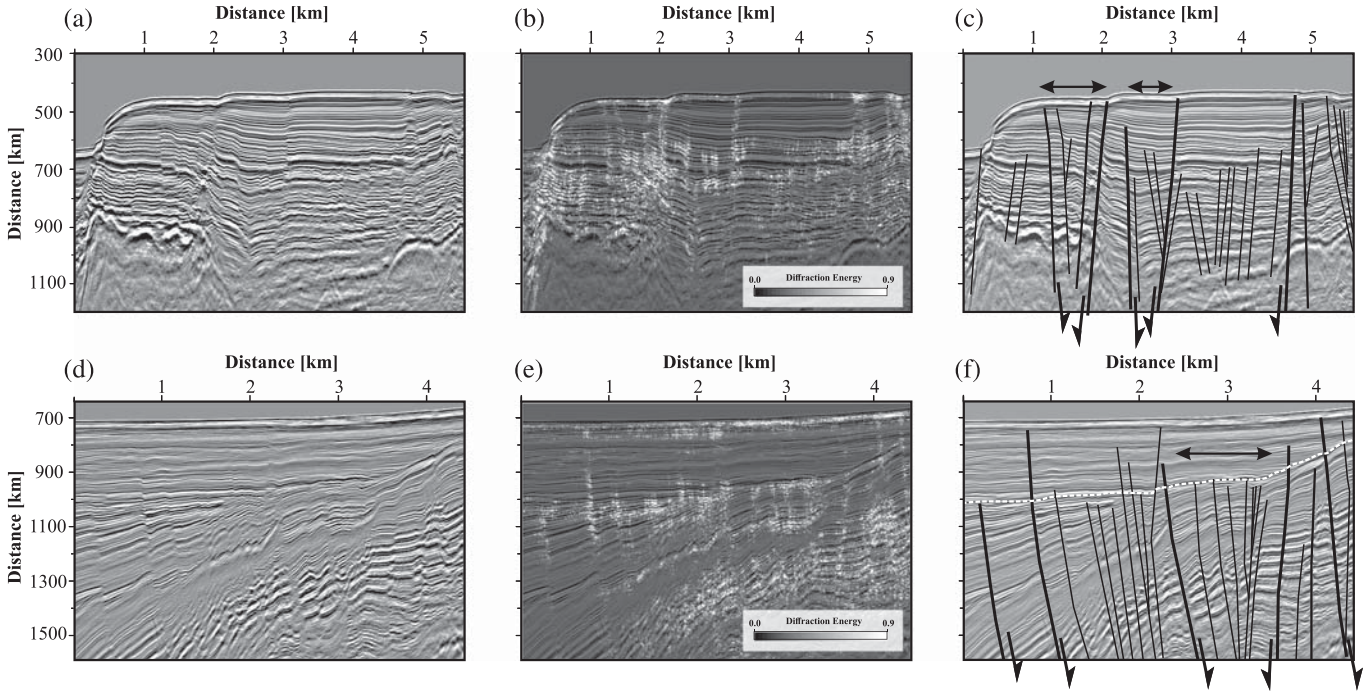

Figure 9. Excerpts of the final depth image of the (a) Astypalaea Plateau and the (d) Santorini-Anafi Basin, (b and e) the respective fault attribute maps, and (c and f) the corresponding fault interpretation. For location, see Figure 8b.

such as the the intrabasinal faults in the Santorini-Anafi Basin (Figures 9d–9f), the diffraction maps provide a powerful guide for the systematic delineation of individual faults.

Based on these images, we present a sketch of the outline of the identified fault systems on the Astypalaea Plateau (Figure 9c) and in the Santorini-Anafi Basin (Figure 9f). In both sections, we identify zones in which the sense of displacement of the faults changes from the NW to the SE forming narrow subsided zones in the center (see arrows in Figures 9c and 9f). On the one hand, these subsidiary faults could be interpreted as forming a part of negative flower structures. Such negative flower structures would be an indication for some form of strike-slip movement (Harding, 1990). On the other hand, the shape of the subsidiary faults could also be explained as the result of antithetic faulting with respect to the marginal Santorini-Anafi Fault. In order to further analyze these narrow zones, however, adjacent seismic lines need to be considered. It is interesting that faulting within the Santorini-Anafi Basin is mostly restricted to the strata below the unconformity highlighted by the dashed line in Figure 9f. This is clearly visible both in the presented diffraction images (Figure 5b) and the fault image (Figure 9e). Only a few faults penetrate the strata above, and their displacement is significantly smaller above than below this unconformity (several meters vs. several tens of meters). This indicates that this unconformity marks a significant change in the tectonic behavior of the fault system. Either the internal faulting within the Santorini-Anafi Basin has ceased mostly after the formation of this unconformity, or the deposition of the upper units has happened very rapidly with regard to the rate of faulting.

In order to further investigate the timing, orientation, and nature of the identified faults, however, adjacent profiles from the POS338 data set have to be taken into account. The internal consistency of the presented results suggests that the proposed diffraction-based workflow for depth imaging is practically feasible and its application to other profiles recorded in the working area is strongly recommended. It was demonstrated that no offset information is required, which makes the vast range of vintage seismic profiles from the SATZ new candidates for resolving the debate on strike-slip deformation in the SATZ shedding new light on the volcano-tectonic evolution of this remarkable morphotectonic zone.

7. Conclusions and Outlook

In this study, we have shown how the diffracted wavefield can be utilized to enable depth conversion of academic seismic data without the need for offset information. Using an offset-limited academic seismic line from the SATZ, we reveal a rich diffracted wavefield by means of a robust separation scheme that models and adaptively subtracts the reflected wavefield from the data. We use the separated diffractions to estimate insightful wavefront attributes and perform wavefront tomography to, for the first time in the study area, derive a depth-velocity model which we use for FD depth migration. The diffraction-based velocity model reliably honors the most prominent features of the seismic profile and accounts for the expected sudden velocity increase at the sediment-basement interface.

We further analyze the quality of the inverted velocity model by examining the focusing of diffractions in a similar manner as CIGs are used in reflection-based processing. Founded on this quality-control scheme, we show that the inverted velocity model is reliable where distinct diffractions from elongated faults are considered as these structures are most likely to lie within the acquisition plane. Here, we were able to validate the inverted velocities at least with an approximate confidence interval of ±15% which we consider acceptable in the context of low-budget academic data. Due to the effect of possible out-of-plane contributions and the partial absence of illumination, however, we identify some areas of the inverted model with geologically implausible velocities. Based on the partial lateral continuity of reflection events, we suggest a complementary knowledge-guided refinement that remains geologically plausible across the full investigated study area.

In addition, we also perform a depth migration of the separated diffracted wavefield to derive spatial diffraction images. These highly resolved reconstructions provide detailed insight into processes like erosion (diffraction at unconformities) or tectonic overprint (diffraction at faults). Following the notion of using the diffraction images as physical attribute maps, a combination with full-wavefield depth images is demonstrated to facilitate the identification of faults and other discontinuous features in depth. Led by these findings, we encourage using the diffracted wavefield for the direct imaging of complicated fault and fracture systems in depth.

The presented depth image allows the first data-based quantification of the thickness distribution of the sedimentary strata as well as fault angles and throws within the SATZ. We estimate a maximum sedimentary thickness of approximately 1,400 m and angles of the marginal faults that indicate normal faulting. Several narrow fault systems identified by means of the unique diffraction depth images in the Santorini-Anafi Basin and on the Astypalaea Plateau appear to be of flower-like assembly. We hypothesize that these features are caused either by zones of narrow strike-slip deformation or antithetic faulting with regard to the listric marginal faults. This movement appears to have been a long-lasting process in the SATZ and is less expressed in the younger sedimentary units.

In conclusion, we strongly encourage the application of the proposed diffraction-based workflow for high-resolution imaging and depth conversion in future studies. Since the presented scheme is likewise applicable to single-channel data, we consider its potential to be very promising, e.g., in the context of scientific drilling where velocities prior to drilling are often only poorly constrained. As was demonstrated by Bauer et al. (2019), diffraction focussing can be directly invoked in wavefront tomography with the benefit of automated quality control and increased stability in complex subsurface settings. Moreover, the challenge of correctly identifying out-of-plane scattering becomes obsolete, if 3D data are considered. Cost-effective limited-offset *P*-cable data are geared toward enabling affordable 3D seismic imaging in academic investigations, which makes this emerging data resource an ideal candidate for diffraction imaging and inversion across scales and communities (Bauer et al., 2020; Planke et al., 2009).

Data Availability Statement

SEG-Y files of the raw prestack data and all intermediate steps (the CMP stack after SRME, reflection-only data, diffraction-only data, diffraction coherency, inverted velocity model, refined velocity model, depth-migrated section, focussed diffractions) are available in the Marine Geoscience Data System with data doi: 10.26022/IEDA/327525. Codes for diffraction-separation and wavefront tomography cannot be provided

in an open repository at the moment since they are the foundation for several future projects the authors are currently working on.

Acknowledgments
The authors want to thank Dirk Gajewski for important discussions and assistance and Paraskevi Nomikou for providing bathymetric data. We further want to thankfully acknowledge the support by Charlotte M. Krawczyk and Geo.X, the geoscientific competence network in Berlin and Potsdam. Insightful comments and suggestions by A. Malehmir, one anonymous reviewer, and the associate editor helped to improve this manuscript. This work was partially funded by the Federal Ministry for Economic Affairs and Energy of Germany (BMWi, 03SX427B) and the German Science Foundation (Deutsche Forschungsgemeinschaft, DFG; HU698/25-1), which also funded the acquisition of the seismic data in 2006 during cruise POS338. In addition, we are grateful to Schlumberger for providing VISTA seismic processing and IHS for providing KINGDOM seismic interpretation software. Open access funding enabled and organized by Projekt DEAL.

References

Bahorich, M., & Farmer, S. (1995). 3-D seismic discontinuity for faults and stratigraphic features: The coherence cube. *The leading edge*, *14*(10), 1053–1058.

Bakhtiari Rad, P., Schwarz, B., Gajewski, D., & Vanelle, C. (2018). Common-reflection-surface-based prestack diffraction separation and imaging. *Geophysics*, *83*(1), S47–S55.

Bauer, A., Schwarz, B., Diekmann, L., & Gajewski, D. (2019). Wavefront tomography with enforced diffraction focusing, *81st EAGE Conference and Exhibition 2019* (Vol. 2019, pp. 1–5). London, UK.

Bauer, A., Schwarz, B., & Gajewski, D. (2016). Enhancement of prestack diffraction data and attributes using a traveltime decomposition approach. *Studia Geophysica et Geodaetica*, *60*(3), 471–486.

Bauer, A., Schwarz, B., & Gajewski, D. (2017). Utilizing diffractions in wavefront tomography. *Geophysics*, *82*(2), R65–R73.

Bauer, A. B., Schwarz, B. S., & Gajewski, D. G. (2018). Diffraction wavefront tomography-efficient automated velocity inversion for multi-fold and single-channel data. In *80th EAGE Conference & Exhibition 2018 Workshop Programme* (pp. cp–556). Copenhagen, Denmark.

Bauer, A., Schwarz, B., & Gajewski, D. (2020). Velocity inversion and scatterer detection with 3D *P*-cable data. *SEG Technical Program Expanded Abstracts 2020*. London, UK.

Berkovitch, A., Belfer, I., Hassin, Y., & Landa, E. (2009). Diffraction imaging by multifocusing. *Geophysics*, *74*(6), WCA75–WCA81.

Bocchini, G. M., Brüstle, A., Becker, D., Meier, T., van Keken, P. E., Ruscic, M., et al. (2018). Tearing, segmentation, and backstepping of subduction in the Aegean: New insights from seismicity. *Tectonophysics*, *734*, 96–118. https://doi.org/10.1016/j.tecto.2018.04.002

Bohnhoff, M., Rische, M., Meier, T., Becker, D., Stavrakakis, G., & Harjes, H. (2006). Microseismic activity in the Hellenic Volcanic Arc, Greece, with emphasis on the seismotectonic setting of the Santorini–Amorgos Zone. *Tectonophysics*, *423*(1–4), 17–33.

Chopra, S., & Marfurt, K. J. (2007). Seismic attributes for prospect identification and reservoir characterization. Society of Exploration Geophysicists and European Association of Geoscientists and Engineers.

Cossette, E., Audet, P., Schneider, D., & Grasemann, B. (2016). Structure and anisotropy of the crust in the Cyclades, Greece, using receiver functions constrained by in situ rock textural data. *Journal of Geophysical Research: Solid Earth*, *121*, 2661–2678. https://doi.org/10.1002/2015JB012460

Dafni, R., & Symes, W. (2017). Diffraction imaging by prestack reverse-time migration in the dip-angle domain. *Geophysical Prospecting*, *65*, 295–316.

Decker, L., Janson, X., & Fomel, S. (2015). Carbonate reservoir characterization using seismic diffraction imaging. *Interpretation*, *3*(1), SF21–SF30.

Dell, S., & Gajewski, D. (2011). Common-reflection-surface-based workflow for diffraction imaging. *Geophysics*, *76*(5), S187–S195.

Diekmann, L., Schwarz, B., Bauer, A., & Gajewski, D. (2019). Source localization and joint velocity model building using wavefront attributes. *Geophysical Journal International*, *219*(2), 995–1007.

Druitt, T., Edwards, L., Mellors, R., Pyle, D., Sparks, R., Lanphere, M., et al. (1999). Santorini volcano. *Geological Society Memoir*, *19*, 49–57.

Druitt, T., & Francaviglia, V. (1992). Caldera formation on santorini and the physiography of the islands in the Late Bronze Age. *Bulletin of Volcanology*, *54*(6), 484–493.

Duveneck, E. (2004). Velocity model estimation with data-derived wavefront attributes. *Geophysics*, *69*(1), 265–274.

Fomel, S. (2002). Applications of plane-wave destruction filters. *Geophysics*, *67*(6), 1946–1960.

Fomel, S., Landa, E., & Taner, M. T. (2007). Poststack velocity analysis by separation and imaging of seismic diffractions. *Geophysics*, *72*(6), U89–U94.

Harding, T. P. (1990). Identification of wrench faults using subsurface structural data: Criteria and pitfalls. *AAPG Bulletin*, *74*(10), 1590–1609.

Heath, B. A., Hooft, E. E. E., Toomey, D. R., Papazachos, C. B., Nomikou, P., Paulatto, M., et al. (2019). Tectonism and its relation to magmatism around Santorini Volcano from upper crustal *P* wave velocity. *Journal of Geophysical Research: Solid Earth*, *124*, 10,610–10,629. https://doi.org/10.1029/2019JB017699

Hooft, E. E. E., Heath, B. A., Toomey, D. R., Paulatto, M., Papazachos, C. B., Nomikou, P., et al. (2019). Seismic imaging of Santorini: Subsurface constraints on caldera collapse and present-day magma recharge. *Earth and Planetary Science Letters*, *514*, 48–61.

Hooft, E., Nomikou, P., Toomey, D., Lampridou, D., Getz, C., Christopoulou, M., et al. (2017). Backarc tectonism, volcanism, and mass wasting shape seafloor morphology in the Santorini-Christiana-Amorgos Region of the Hellenic Volcanic Arc. *Tectonophysics*, *712*, 396–414.

Hübscher, C., Hensch, M., Dahm, T., Dehghani, A., Dimitriadis, I., Hort, M., & Taymaz, T. (2006). Toward a risk assessment of central Aegean volcanoes. *Eos, Transactions American Geophysical Union*, *87*(39), 401–407.

Hübscher, C., Ruhnau, M., & Nomikou, P. (2015). Volcano-tectonic evolution of the polygenetic Kolumbo submarine volcano/Santorini (Aegean Sea). *Journal of Volcanology and Geothermal Research*, *291*, 101–111.

Jäger, R., Mann, J., Höcht, G., & Hubral, P. (2001). Common-reflection-surface stack: Image and attributes. *Geophysics*, *66*(1), 97–109.

Karimpouli, S., Malehmir, A., Hassani, H., Khoshdel, H., & Nabi-Bidhendi, M. (2015). Automated diffraction delineation using an apex-shifted Radon transform. *Journal of Geophysics and Engineering*, *12*(2), 199–209.

Landa, E., & Keydar, S. (1998). Seismic monitoring of diffraction images for detection of local heterogeneities. *Geophysics*, *63*(3), 1093–1100.

Le Pichon, X., & Angelier, J. (1979). The Hellenic arc and trench system: A key to the neotectonic evolution of the eastern Mediterranean area. *Tectonophysics*, *60*(1-2), 1–42.

Le Pichon, X., & Kreemer, C. (2010). The miocene-to-present kinematic evolution of the eastern Mediterranean and middle east and its implications for dynamics. *Annual Review of Earth and Planetary Sciences*, *38*, 323–351.

Malehmir, A., Schmelzbach, C., Bongajum, E., Bellefleur, G., Juhlin, C., & Tryggvason, A. (2009). 3D constraints on a possible deep >2.5 km massive sulphide mineralization from 2D crooked-line seismic reflection data in the Kristineberg mining area, northern Sweden. *Tectonophysics*, *479*(3-4), 223–240.

Marfurt, K. J., Kirlin, R. L., Farmer, S. L., & Bahorich, M. S. (1998). 3-D seismic attributes using a semblance-based coherency algorithm. *Geophysics*, *63*(4), 1150–1165.

Morgan, J., Warner, M., Bell, R., Ashley, J., Barnes, D., Little, R., et al. (2013). Next-generation seismic experiments: Wide-angle, multi-azimuth, three-dimensional, full-waveform inversion. *Geophysical Journal International*, *195*(3), 1657–1678.
Moser, T., & Howard, C. (2008). Diffraction imaging in depth. *Geophysical Prospecting*, *56*(5), 627–641.
Neidell, N. S., & Taner, M. T. (1971). Semblance and other coherency measures for multichannel data. *Geophysics*, *36*(3), 482–497.
Nomikou, P., Druitt, T. H., Hübscher, C., Mather, T. A., Paulatto, M., Kalnins, L. M., et al. (2016). Post-eruptive flooding of Santorini caldera and implications for tsunami generation. *Nature communications*, *7*(1), 1–10.
Nomikou, P., Hübscher, C., & Carey, S. (2019). The Christiana-Santorini-Kolumbo volcanic field. *Elements*, *15*, 171–176.
Nomikou, P., Hübscher, C., Papanikolaou, D., Farangitakis, G. P., Ruhnau, M., & Lampridou, D. (2018). Expanding extension, subsidence and lateral segmentation within the Santorini-Amorgos basins during quaternary: Implications for the 1956 amorgos events, central-south Aegean Sea, Greece. *Tectonophysics*, *722*, 138–153.
Nomikou, P., Hübscher, C., Ruhnau, M., & Bejelou, K. (2016). Tectono-stratigraphic evolution through successive extensional events of the Anydros Basin, hosting Kolumbo volcanic field at the Aegean Sea, Greece. *Tectonophysics*, *671*, 202–217.
Nomikou, P., Papanikolaou, D., Alexandri, M., Sakellariou, D., & Rousakis, G. (2013). Submarine volcanoes along the Aegean volcanic arc. *Tectonophysics*, *597*, 123–146.
Nunns, A. G. (1991). Structural restoration of seismic and geologic sections in extensional regimes (1). *AAPG bulletin*, *75*(2), 278–297.
Perissoratis, C. (1995). The santorini volcanic complex and its relation to the stratigraphy and structure of the Aegean arc, Greece. *Marine Geology*, *128*(1–2), 37–58.
Planke, S., Eriksen, F. N., Berndt, C., Mienert, J., & Masson, D. G. (2009). *P*-cable high-resolution seismic. *Oceanography*, *22*(1), 85.
Sakellariou, D., Sigurdsson, H., Alexandri, M., Carey, S., Rousakis, G., Nomikou, P., et al. (2010). Active tectonics in the Hellenic volcanic arc: The Kolumbo submarine volcanic zone. *Bulletin of the Geological Society of Greece*, *43*(2), 1056–1063.
Schwarz, B. (2019a). Coherent wavefield subtraction for diffraction separation. *Geophysics*, *84*(3), V157–V168.
Schwarz, B. (2019b). An introduction to seismic diffraction. *Advances in Geophysics*, *60*, 1–64.
Schwarz, B., Bauer, A., & Gajewski, D. (2016). Passive seismic source localization via common-reflection-surface attributes. *Studia Geophysica et Geodaetica*, *60*(3), 531–546.
Schwarz, B., & Gajewski, D. (2017). Accessing the diffracted wavefield by coherent subtraction. *Geophysical Journal International*, *211*(1), 45–49.
Silvestrov, I., Baina, R., & Landa, E. (2015). Poststack diffraction imaging using reverse-time migration. *Geophysical Prospecting*, *64*(1), 129–142.
Tsampouraki-Kraounaki, K., & Sakellariou, D. (2018). Seismic stratigraphy and geodynamic evolution of Christiana Basin, South Aegean arc. *Marine Geology*, *399*, 135–147.
Verschuur, D. J., Berkhout, A. J., & Wapenaar, C. P. A. (1992). Adaptive surface-related multiple elimination. *Geophysics*, *57*(9), 1166–1177.
Virieux, J., & Operto, S. (2009). An overview of full-waveform inversion in exploration geophysics. *Geophysics*, *74*(6), WCC1–WCC26.
Warner, M., Ratcliffe, A., Nangoo, T., Morgan, J., Umpleby, A., Shah, N., et al. (2013). Anisotropic 3D full-waveform inversion. *Geophysics*, *78*(2), R59–R80.
Yin, J., & Nakata, N. (2017). Diffraction imaging with geometric-mean reverse time migration, *SEG Technical Program Expanded Abstracts 2017* (pp. 974–979). London, UK: Society of Exploration Geophysicists.